CrossMark

ORIGINAL PAPER

Influence of post-calcination treatment on the spinel lithium titanium oxide anode material for lithium ion batteries

Jie Liu[1,2] · Ke-jun Deng[1] · Chen-ge Yang[1] · Bo Liu[1] · Chang Li[1] · Zhen-hui Yao[1] · Ling Su[1]

Abstract The influence of post-calcination treatment on spinel $Li_4Ti_5O_{12}$ anode material is extensively studied combining with a ball-milling-assisted rheological phase reaction method. The post-calcinated $Li_4Ti_5O_{12}$ shows a well distribution with expanded gaps between particles, which are beneficial for lithium ion mobility. Electrochemical results exhibit that the post-calcinated $Li_4Ti_5O_{12}$ delivers an improved specific capacity and rate capability. A high discharge capacity of 172.9 mAh g^{-1} and a reversible charge capacity of 171.1 mAh g^{-1} can be achieved at 1 C rate, which are very close to its theoretical capacity (175 mAh g^{-1}). Even at the rate of 20 C, the post-calcinated $Li_4Ti_5O_{12}$ still delivers a quite high charge capacity of 124.5 mAh g^{-1} after 50 cycles, which is much improved over that (43.9 mAh g^{-1}) of the pure $Li_4Ti_5O_{12}$ without post-calcination treatment. This excellent electrochemical performance should be ascribed to the post-calcination process, which can greatly improve the lithium ion diffusion coefficient and further enhance the electrochemical kinetics significantly.

✉ Jie Liu
DearLuos@Hotmail.com

[1] Chongqing ChangAn New Energy Automobile Co. Ltd, Chongqing 401120, People's Republic of China

[2] Department of Applied Chemistry, School of Chemical Engineering and Technology, Tianjin University, Tianjin 300072, People's Republic of China

Introduction

$Li_4Ti_5O_{12}$ (LTO), a composite oxide with a spinel-type lattice structure, has been considered as the most promising anode material for high power density lithium ion batteries due to its unique advantages, such as reliable safety performance, ideal cyclability, and environmental friendliness [1, 2]. As we know, the fact that a good electrode material for lithium-ion battery should have both good electronic conductivity and considerable Li$^+$ ion diffusion coefficient [3]. Unfortunately, as an insulator, LTO presents a very low electronic conductivity which is unfavorable to fast reaction rates (high power) for the lithium-ion battery, thus result in the depressing rate capability, and greatly hinder its practical application [4–6]. To conquer this problem, numerous strategies have been developed to improve the rate capability of LTO electrodes, including the crystallite size reduction [7], doping with guest atoms [8, 9], and surface modification [10, 11]. Concretely, reducing particle size can improve the rate capability effectively because small particle size shortens the distance of electron conduction and lithium ion transportation within the particles. Structural doping with foreign ions can enhance the electronic/ionic conductivity in LTO particles; however, it can increase the existence of defects as well, which is detrimental: Octahedral defects (16d) reduce the capacity, and tetrahedral defects (8a) generate an irreversible insertion capacity loss [12]. Besides, surface modification, especially the carbon coating, is seen the most effective method to improve the electrochemical properties of LTO. Nevertheless, a high amount of inactive coating materials definitely decrease the tap density of active material and reduce the electrode capacity significantly, and thus decrease the energy density though they can improve the electronic conductivity to some extent [13]. On the other hand, it is not in favor of upscaling process of the electrode in the actual production process and the active

Springer

material can easily fall off the copper/aluminum foil for the nano-carbon-coated LTO. Therefore, it is urgent to develop a new strategy, which is easy for industrial processing and beneficial for the electronic/ionic conductivity without sacrificing the energy density of LTO anode material. Herein, a simple "post-calcination treatment" strategy is put forward to improve the electrochemical performance of LTO. The specific approach is that the carbon-coated LTO was prepared first via an in situ carbon coating process, and then the residual carbon was burnt out in a short time. By this method, the grain growth of LTO can be suppressed during the pyrolysis process by the film of amorphous carbon which acts as a diffusion barrier [14]. Meanwhile, the spacing between particles can be expanded after driving out the carbon, which is beneficial for the infiltration of electrolyte thereby strengthening the lithium ion diffusion.

Up to now, many methods have been adopted for the synthesis of LTO material, including solid-state method [15, 16], sol-gel method [17–19], combustion synthesis [20, 21], and microwave-assisted synthesis [22–24]. However, all the methods mentioned above are limited by long reactive time, complicated operations, or unmanageable reaction conditions, more or less. Another novel soft chemistry synthesis method, rheological phase reaction method, is widely investigated recently, which can be regarded as a development of the conventional solid-state method [25, 26]. By which the solid-liquid rheological mixture contacts the reactants closely and uniformly regardless of their solubility, thus the heat and mass transfer between the solid particle and fluid can be carried out easily and quickly. More importantly, this method satisfies the requirements of industrialization, including low material cost, short calcination time, no sophisticated apparatus, and easy to scale-up.

In this paper, a modified rheological phase reaction method was employed to synthesize carbon-coated LTO in N_2 flow, and the post-calcined LTO was obtained after a following calcination process in air atmosphere. The structure, morphology, particle size distribution, and the electrochemical performance of the as-synthesized samples were investigated in detail. In addition, the electrochemical results manifest that the post-calcined LTO delivers a high lithium ion diffusion coefficient and improved rate capability.

Experimental

Materials preparation

The in situ carbon-coated LTO nano-powders were prepared via a ball-milling-assisted rheological phase reaction method using titanium dioxide (anatase TiO_2, 10 nm), lithium carbonate (Li_2CO_3, AR.) and citric acid ($C_6H_8O_7·H_2O$, AR.) as the raw materials, where the citric acid served as dispersing agent

and carbon source. At first, 2.6095 g TiO_2, 1.0138 g Li_2CO_3, and 0.8748 g $C_6H_8O_7·H_2O$ were mixed and scattered over a certain amount of ethanol and then ball-milled for 6 h to form a rheological mixture. Secondly, the rheological mixture was dried at 80 °C and preheated at 400 °C for 4 h in N_2 atmosphere to get the precursor. Finally, the obtained precursor was ground and calcined at 800 °C for 12 h in N_2 flow to obtain the carbon-coated LTO (CC-LTO). In addition, the carbon content of CC-LTO is 3.24 wt%, as confirmed by a CHN analyzer. Subsequently, a part of CC-LTO sample was further heat-treated at 600 °C for 1 h to drive out the carbon, and the resulting product was the called post-calcined LTO (PC-LTO). For a comparison, the pure LTO (SS-LTO) sample without post-calcination process was also synthesized by a conventional solid-state method with the addition of $C_6H_8O_7$ and calcined in air directly.

Materials characterization

The crystal structure of as-synthesized SS-LTO, CC-LTO, and PC-LTO was examined by X-ray diffraction (XRD) with a Rigaku RINT2000 instrument equipped with Cu Kα radiation. The XRD data were collected by using a step scan method in the range of 10–80°, and the step size is 0.02° and scan time is 1 s. The EXPGUI interface for the GSAS was used for Rietveld refinements. Raman spectra were measured using Jobin Yvon T64000 system and Nd: YAG laser (wavelength 532 nm; maximum power 2 mW). The morphology of samples was observed by scanning electron microscope (Hitachi S4800) (SEM). The post-calcination process was examined by thermogravimetric analysis and differential scanning calorimetry (TG-DSC) using the Netzsch STA 449F thermal analyzer in static air at a heating rate of 10 °C min^{-1}. The size distribution of the powders was identified by a laser particle size analyzer (Beckman, Delsa Nano C). Transmission electron microscopy (TEM) studies of the samples were carried out by using a JEM-2100F transmission electron microscope operated at 200 kV. Nitrogen adsorption/desorption measurements were performed with a Belsorp-mini II apparatus (BEL Inc., Osaka, Japan) to determine Brunauer-Emmett-Teller (BET) surface areas. And the pore size distribution was calculated by the Barret-Joyner-Halenda (BJH) method.

Electrochemical measurements

The working electrodes were prepared by using 80 wt% of active materials, 10 wt% super-P, and 10 wt% polyvinylidene difluoride (PVDF) dissolved in N-methyl-2-pyrrolidine. And the obtained slurries were then daubed on aluminum foils, dried at 120 °C in a vacuum oven for 12 h. The coin cells (CR2032) were fabricated using the lithium foils as counter electrodes and reference electrodes. The electrolyte was 1-M solution of $LiPF_6$ in a mixture of ethylene carbonate (EC) and

diethyl carbonate (DEC) (1:1 in volume). And polypropylene (Celgard® 2300, Celgard LLC, Charlotte, NC) was used as the separator. The cells were assembled in an argon-filled glove box by keeping both the moisture content and oxygen level less than 5 ppm.

The cyclic voltammetry (CV) tests were carried out on an electrochemical workstation (CHI1040B, ChenHua, China) at a scanning rate of 0.1 mV s^{-1} in the voltage range of 1.0–3.0 V (vs. Li/Li$^+$). And the charge/discharge measurements were performed in the voltage range of 1.0–3.0 V (vs. Li/Li$^+$) at different rates on an automatic batteries tester (Land CT 2001 A, Wuhan, China). The electrochemical impedance spectroscopy (EIS) was measured by an electrochemical workstation (GAMRY PC14–750) in the frequency range from 100 kHz to 10 mHz. All the electrochemical performances were tested at constant temperature of 25 °C.

Results and discussion

Figure 1a shows the XRD patterns of the as-prepared SS-LTO, CC-LTO, and PC-LTO anode materials. It can be found that all the diffraction peaks of samples can be readily indexed to the spinel LTO (cubic phase, space group $Fd\text{-}3m$, PDF# 49-0207), and no obvious impurity phase can be detected. Moreover, the sharp diffraction peaks and strong diffraction intensities indicate the good crystallinity of the samples. Figure 1b–d presents the observed, calculated, and error patterns for the SS-LTO, CC-LTO, and PC-LTO anode materials, and the corresponding refined results are summarized in Table 1. As indicated, the lattice parameters of SS-LTO and PC-LTO samples are substantially identical, while CC-LTO has a much smaller lattice parameter. This variation can be attributed to a change in the crystallinity of the CC-LTO sample, which is altered with the change of stress by the carbon-coating process [27].

In order to further investigate the influence of post-calcination, the SS-LTO, CC-LTO, and PC-LTO samples were examined by Raman spectroscopy. As shown in Fig. 2a, the Raman spectra features agree well with the typical $Li_{4/3}Me_{5/3}O_4$ spinel spectra, which show all five active Raman phonon modes $(A_{1g} + E_g + 3F_{2g})$ [28–30]. In particular, the mode observed at 431 cm^{-1} can be assigned to the Li–O stretching vibrations. Also, a strong band at 672 cm^{-1} with the shoulder at 752 cm^{-1} can be viewed as the stretching vibrational mode of Ti–O covalent bonding in TiO$_6$ octahedra [29–31]. Moreover, the
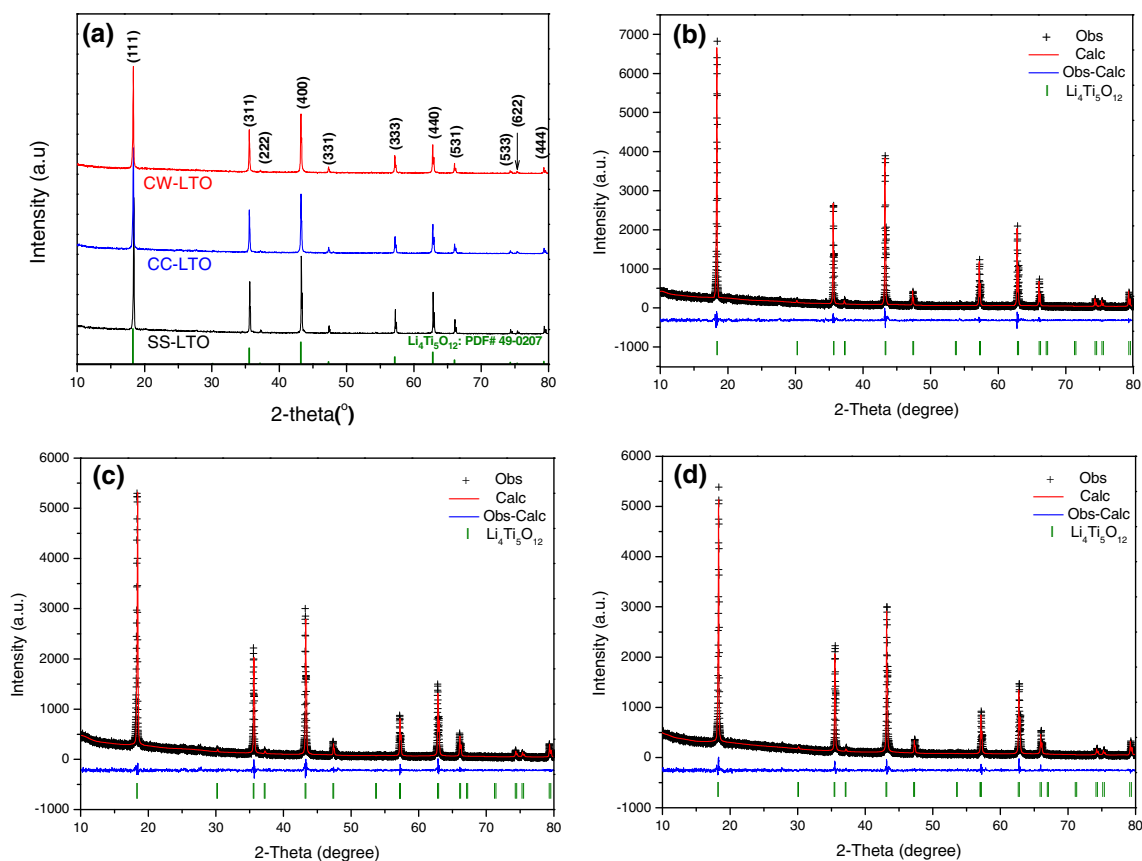

Fig. 1 **a** X-ray diffraction patterns of the as-synthesized SS-LTO, CC-LTO, and PC-LTO samples. Rietveld refinement results for **b** SS-LTO, **c** CC-LTO, and **d** PC-LTO. *SS-LTO* pure LTO prepared by a conventional solid-state method, *CC-LTO* carbon-coated LTO, *PC-LTO* post-calcinated LTO

Table 1 Rietveld analysis results for the SS-LTO, CC-LTO, and PC-LTO samples

Sample	a (Å)	R_{wp}	R_p	χ^2
SS-LTO	8.361060	0.0787	0.0659	1.388
CC-LTO	8.357093	0.0775	0.0653	1.214
PC-LTO	8.361073	0.0729	0.0634	1.099

Raman bands corresponding to the Li–O and Ti–O vibrations are shifted toward the low-wavenumber side after the post-calcination process. This phenomenon indicates the change of mechanic strength, which agrees well with the XRD refinement results as given above. It is worth mentioning that the Raman spectrum recorded after post-calcination process shows some additional Raman bands around 522 and 584 cm^{-1}, which is probably due to the increased imperfection and disorder in the crystal structure [32, 33]. Additionally, as shown in Fig. 2b, two intense broad peaks at about 1346 and 1593 cm^{-1} are observed in the Raman spectrum of CC-LTO, which are ascribed to the D and G bands of pyrolytic carbon in the CC-LTO sample, respectively [34]. In sharp contrast, there is no Raman signal in the same range for the PC-LTO sample, indicating that the carbon in the CC-LTO has been completely removed after the post-calcination process.

Scanning electron microscopy (SEM) images of SS-LTO, CC-LTO, and PC-LTO samples are shown in Fig. 3. It can be seen that the SS-LTO sample has a larger particle size than that of the CC-LTO and PC-LTO samples. Regarding to this difference, it should be attributed to the pyrolytic carbon which performs as a diffusion barrier to inhibit the grain growth of LTO and thus leads to a decrease of crystallite size for the CC-LTO sample. In addition, the particles do not grow up obviously after a heat treatment at 600 °C for 1 h, as shown in Fig. 3c, c'. Discovered through comparative analysis, the PC-LTO sample demonstrates more deep pores than the SS-LTO and CC-LTO samples. The deep pores, marked by small

yellow circles in Fig. 3c, c', can be attributed to the post-calcination treatment, as illustrated in Fig. 4. Driving out of the carbon enlarges the gaps between LTO particles; moreover, the gas of CO_2 resulted from the combustion of carbon can also produce many one-dimensional channels during its diffusion process, which are advantageous to the lithium ion diffusion for the PC-LTO anode material. TG–DSC curves of the CC-LTO are presented in Fig. 5. The first weight loss stage on the TG curve corresponds to evaporation of water within the range from ambient temperature to around 200 °C. The weight loss from 200 to 600 °C should be due to the combustion of carbon, accompanied with the obvious endothermic peak at 442.3 °C on the DSC curve. Moreover, the TG analysis reveals that the carbon content in the CC-LTO was approximately 3.35 wt%, which agrees well with the result of CHN analyzer as given above.

The particles are identified by a laser particle size analyzer, and the results are depicted in Fig. 6 and listed in Table 2. The samples were ultrasonically treated for 1 h before testing. As shown in Fig. 6, each of the three samples delivers a concentrated particle size distribution, suggesting that rheological phase reaction is a promising method to prepare electrode materials without obvious agglomeration. Furthermore, the average diameters of SS-LTO, CC-LTO, and PC-LTO are 93.98, 33.24, and 46.51 nm, respectively. The results indicate that the pyrolytic carbon which results from citric acid can suppress the grain growth effectively and the small particle diameter can be maintained even after a further calcining process at 600 °C for 1 h. Similar to SEM observations and particle size analysis, TEM images can also confirm the effect of post-calcination. As indicated from Fig. 7, the particles of CC-LTO anode material are closely packed, while the PC-LTO particles distribute loosely with many gaps. For instance, it can be clearly observed from Fig. 7b that the gaps and pores of CC-LTO sample are packed with particles and/or amorphous carbon. In sharp contrast, the gaps between the PC-LTO nanoparticles, as shown in Fig. 7d, are much larger than
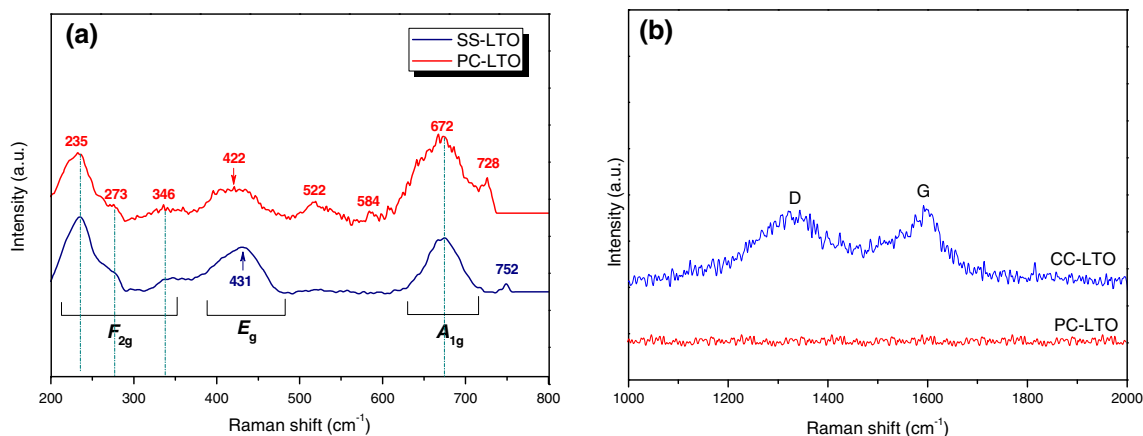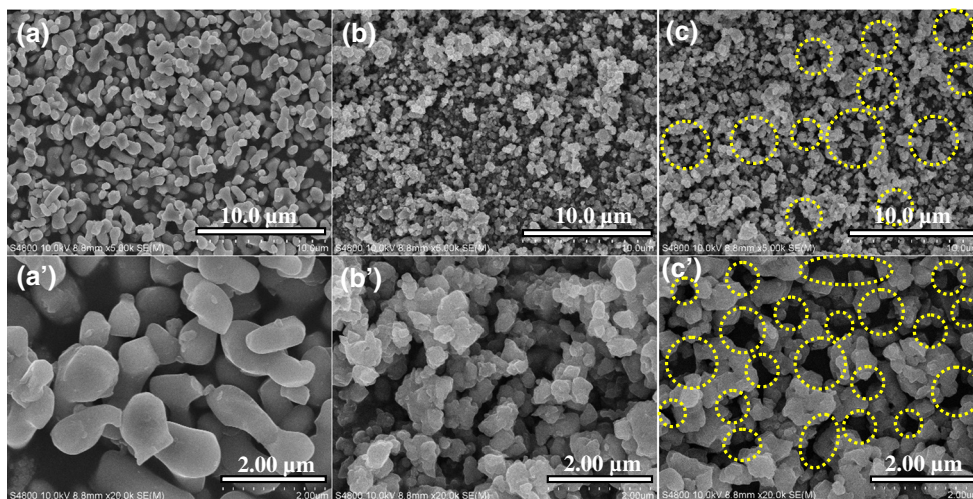

Fig. 2 Raman spectra of the SS-LTO and PC-LTO samples in the ranges of **a** 200–800 and **b** 1000–2000 cm^{-1}

Fig. 3 SEM images of the samples: **a**, **a'** SS-LTO, **b**, **b'** CC-LTO, and **c**, **c'** PC-LTO. The *areas circled with small yellow circles* represent the deep pores resulted from the post-calcination treatment, which are beneficial for Li$^+$ diffusion

those of CC-LTO sample, indicating wider lithium ion diffusion space over the CC-LTO sample.

For a clearer understanding of the mesoporosity, the nitrogen-adsorption measurements were employed. The nitrogen adsorption-desorption isotherms of CC-LTO and PC-LTO samples are shown in Fig. 8, which exhibit a typical IV-type curve with a small hysteresis loop at higher relative pressure, indicating a wide range of pore size distribution [35]. As shown in the inserts, the pore volume of CC-LTO and PC-LTO samples calculated from the adsorption quantity with relative pressure $p/p_0 = 0.99$ using the Barrett-Joyner-Halenda (BJH) method are 0.0502 and 0.0639 mL g^{-1}, and the average pore diameters are 96.9 and 140.0 Å, respectively. The pore size distributions indicate that the average mesoporous size of PC-LTO is larger than that of CC-LTO, which is facilitated more electrolyte penetrating into the particle interior and provide wider transmission channels which allow more Li$^+$ diffusion simultaneously [36]. This comment is well consistent with the results of SEM and TEM analyses mentioned above.

The electrochemical performance tests were studied by employing 2032 coin-type half cells. Figure 9a presents the second charge/discharge curves of SS-LTO, CC-LTO, and PC-LTO samples at 1 C rate. Each sample delivers a couple of stable charge-discharge potential plateaus of ~1.55 V (vs. Li/Li$^+$), which is closely related to the Ti^{4+}/Ti^{3+} redox couple. It can be seen that the CC-LTO and PC-LTO samples exhibit

much better charge-discharge performance than that of SS-LTO. Especially, the PC-LTO sample delivers the highest specific capacity of the three samples, which achieves a discharge capacity of 172.9 mAh g^{-1} and a reversible charge capacity of 171.1 mAh g^{-1} at 1 C, very close to its theoretical capacity (175 mAh g^{-1}). This improved electrochemical performance should be ascribed to the reduced particle size and the porous structure resulted from the post-calcination process.

Cyclic voltammetry properties of SS-LTO, CC-LTO, and PC-LTO electrodes for the second cycle at a scan rate of 0.1 mV s^{-1} between 1.0 and 3.0 V are shown in the inset of Fig. 9a. For each sample, besides the common cathodic peak which lies at around 1.5 V, another shoulder peak located at around 1.42 V can also be observed. This phenomenon usually appears in nano-sized LTO due to the existence of faradaic pseudocapacitance [37–39]. According to previous studies [40, 41], the pseudocapacitive reaction is a quick lithium ion insertion process and brings on an extra capacity. Thus, the pseudocapacitive effect is advantageous to improve the specific capacity and high-rate capability. In addition, the separation between anodic and cathodic peak (the higher one)
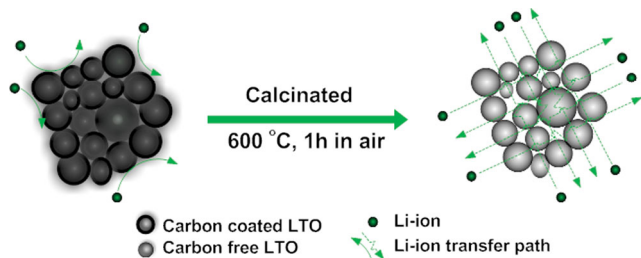

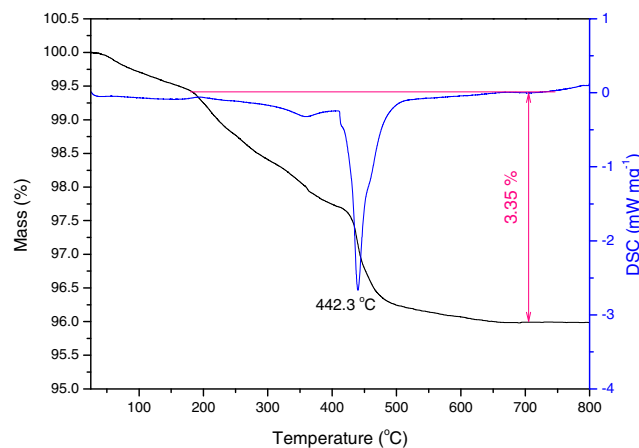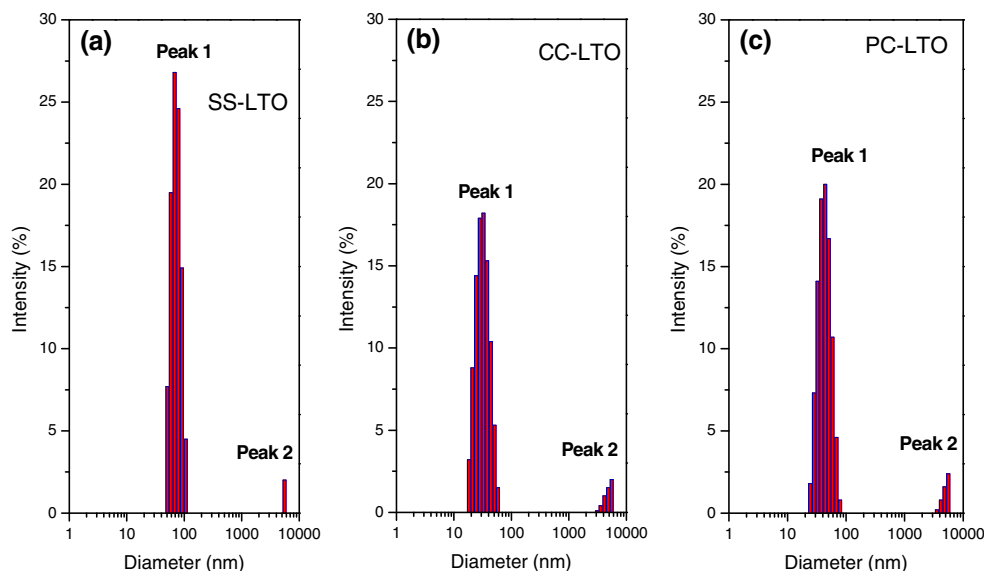**Fig. 4** Schematic illustration of the post-calcination process

Fig. 5 Thermogravimetry (TG) and differential scanning calorimetry (*DSC*) curves of CC-LTO

Fig. 6 Particle size distribution of the as-synthesized **a** SS-LTO, **b** CC-LTO, and **c** PC-LTO

potentials is 245 mV for the SS-LTO, while the values for CC-LTO and PC-LTO samples are 208 and 212 mV, respectively. The lower potential differences for CC-LTO and PC-LTO indicate the less polarizations, which should be attributed to the smaller grain size, as given by the SEM and particle size analyses above. Fortunately, for the PC-LTO, the polarization does not increase notably after the post-calcination process, suggesting that the intercalation and deintercalation of lithium ion are highly reversible.

To evaluate the rate capabilities of the as-synthesized SS-LTO, CC-LTO, and PC-LTO anode materials, the electrodes were cycled at different current rates in a stepped mode, from 1 C increased to 20 C and then reduced to 1 C, as shown in Fig. 6b. Both the three samples exhibit excellent cycling stability at different charge/discharge current rates. This indicates that the integrated structure of the composite has been maintained even after high rate charge/discharge processes, which is a promising characteristic required for high power applications. What's more, it can be found that PC-LTO delivers the highest charge specific capacities of all the three samples at each current rate. Specifically, the PC-LTO anode material exhibits a large charge capacity of 172.2 mAh g^{-1} after 10 cycles at 1 C rate. Even at a high rate current of 20 C, it still delivers a stable and high capacity of 124.5 mAh g^{-1} after 50 cycles. For comparison, the CC-LTO sample, without

driving out the carbon, shows relatively lower capacities and the corresponding capacities are 163.4 and 112.9 mAh g^{-1} at 1 and 20 C, respectively. However, in sharp contrast, the SS-LTO counterpart shows a very disappointing capacity of only 43.9 mAh g^{-1} at 20 C. Clearly, the post-calcination treatment has significantly improved the rate capability of LTO anode. Thus, here, the rate capability of LTO anode material is mainly determined by its particle size, electrical conduction between particles, and lithium ion diffusion coefficient.

Figure 9c demonstrates the rate performance of PC-LTO at various rates. The charge specific capacities are 171.2, 161.3, 156.6, 141.7, and 128.1 mAh g^{-1} at 1, 3, 5, 10, and 20 C, respectively, which correspond to the ladder cycling results showed in Fig. 9b. It is worth noting that another potential platform in the discharge curves can be observed gradually with the increase of the current rate. This phenomenon should be ascribed to the pseudocapacitive effect, which agrees well with the results of CV curves given above. Figure 9d presents the long-term cycling performance for the PC-LTO electrode. As indicated, the charge specific capacities of 167.9, 156.8, 151.3, and 132.2 mAh g^{-1} can be retained at 1, 3, 5, and 10 C after 100 cycles, with the capacity retention of 98.2, 97.2, 96.7, and 93.4 %, respectively. The superior charge capacity and rate capability of PC-LTO suggest that the post-calcination method is a promising strategy to improve the electrochemical kinetics.

In order to further study the effectiveness of post-calcination, EIS was performed and the Nyquist plots are shown in Fig. 10a. The AC impedance spectra were fitted with the aid of an equivalent circuit, as given in the inset of Fig. 10a, where R_s and R_{ct} represent the resistance of electrolyte and the charge-transfer resistance at the active interface, respectively. CPE, namely the constant phase element, reflects the interfacial capacitance. Z_w embodies the Warburg impedance describing lithium ion diffusion in the bulk electrode. The main

Table 2 Values of the particle size for the as-synthesized SS-LTO, CC-LTO, and PC-LTO samples

Sample	Peak 1 (*d. nm*)	Peak 2 (*d. nm*)	Average (*d. nm*)
SS-LTO	72.81	5560	93.98
CC-LTO	32.50	4834	33.24
PC-LTO	43.73	5017	46.51

Fig. 7 TEM images of the **a**, **b** CC-LTO and **c**, **d** PC-LTO samples
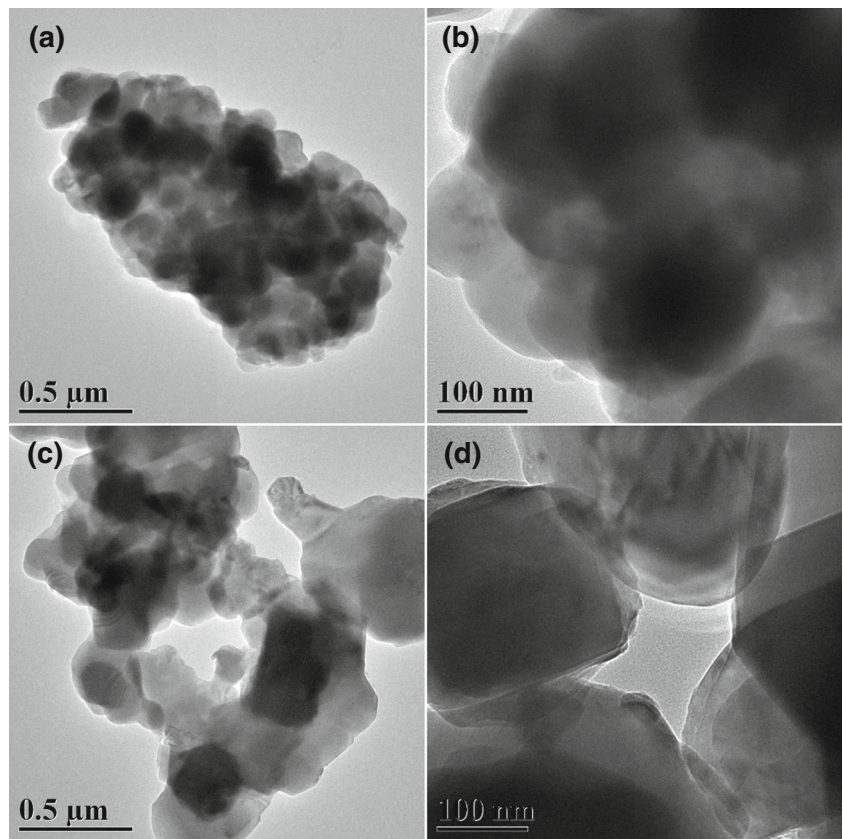
parameters of the equivalent circuit for all the samples are listed in Table 3. It can be seen that the R_s values of different samples are smaller than 4 Ω. And, the differences of these R_s values may be interpreted in terms of simulated errors [6]. However, the R_{ct} values largely vary with different samples and the CC-LTO anode material delivers the lowest value, confirming the reduced charge-transfer resistance which is due to the small particle size and in situ carbon coating. Besides, the R_{ct} value of PC-LTO sample is only 16.37 Ω larger than that of CC-LTO, indicating that the electronic conductivity is still considerable after driving out the carbon.

The lithium ion diffusion coefficient (D) could be calculated from the low frequency plots according to the following equations [42]:

$$Z_{re} = R_s + R_{ct} + \sigma\omega^{-\frac{1}{2}} \tag{1}$$

$$D = \frac{R^2 T^2}{2A^2 n^4 F^4 C_{Li}^2 \sigma^2} \tag{2}$$

where Z_{re}, R, T, A, n, F, and C_{Li} are the real part of impedance, gas constant, absolute temperature (298.15 K), surface area (0.785 cm^2), number of electrons transferred in the half-
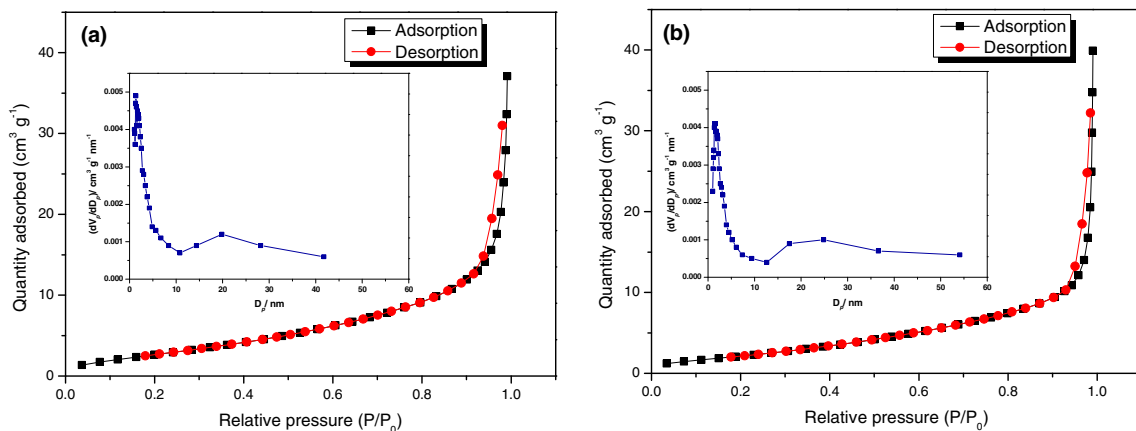

Fig. 8 Nitrogen adsorption-desorption isotherms of **a** CC-LTO and **b** PC-LTO samples. The *insets* are the corresponding pore size distribution curves determined by the BJH method
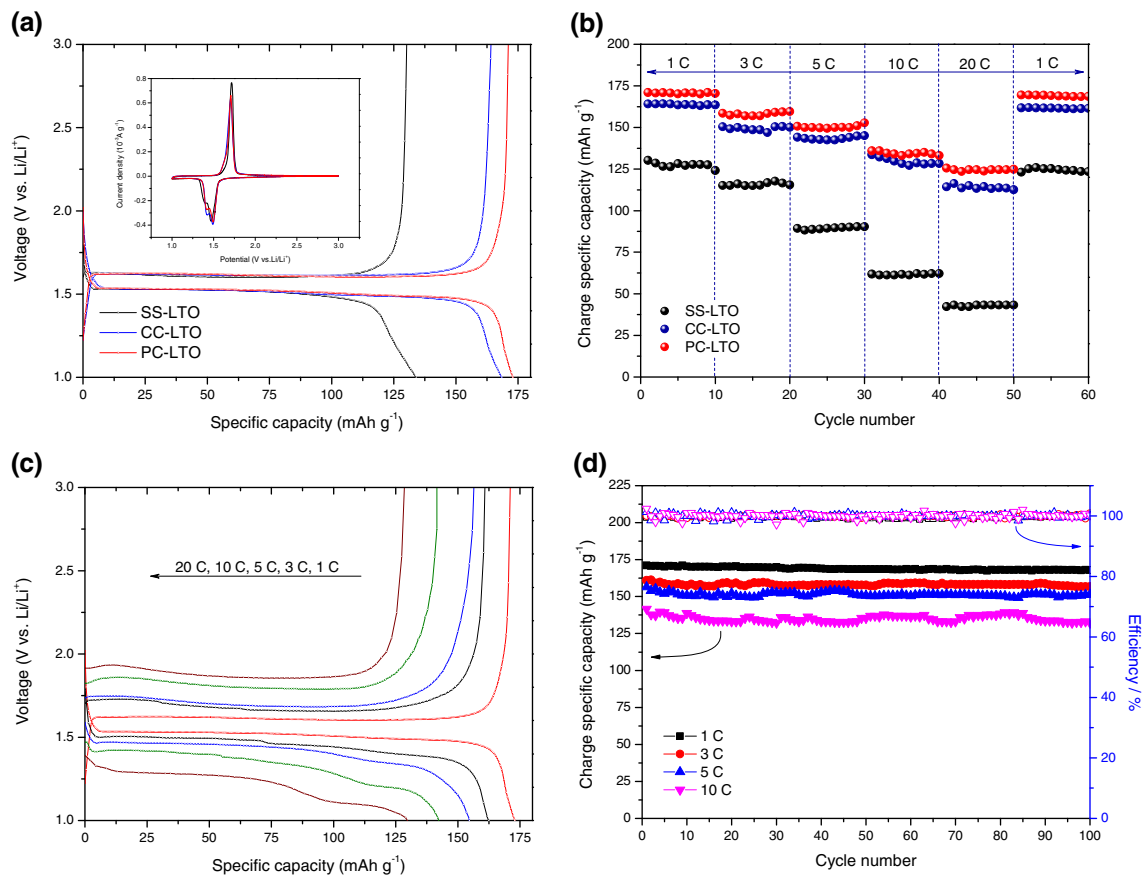
Fig. 9 a The second charge/discharge profiles of SS-LTO, CC-LTO, and PC-LTO anode materials at 1 C rate. *Inset* is the CV curves for the samples for the second cycle in the voltage range of 1.0–3.0 V at a scan rate of 0.1 mV s^{-1}.

b Rate capability of SS-LTO, CC-LTO, and PC-LTO electrodes. **c** The second charge/discharge profiles of PC-LTO at different current rates and **d** long-term cycling performance for PC-LTO at 1, 3, 5, and 10 C

reaction for the redox couple, Faraday constant, and molar concentration of lithium ions in solid (4.37 × 10^{-3} mol cm^{-3} [43]), respectively. σ is the Warburg factor, which is relative to Z_{re}, and the Z_{re}–$\omega^{-1/2}$ plots are presented in Fig. 10b.

The lithium ion diffusion coefficients of the SS-LTO, CC-LTO, and PC-LTO electrodes are calculated according to Eq. (2) and given in Table 3. It is obvious that the lithium ion diffusion coefficient increases due to the post-calcination
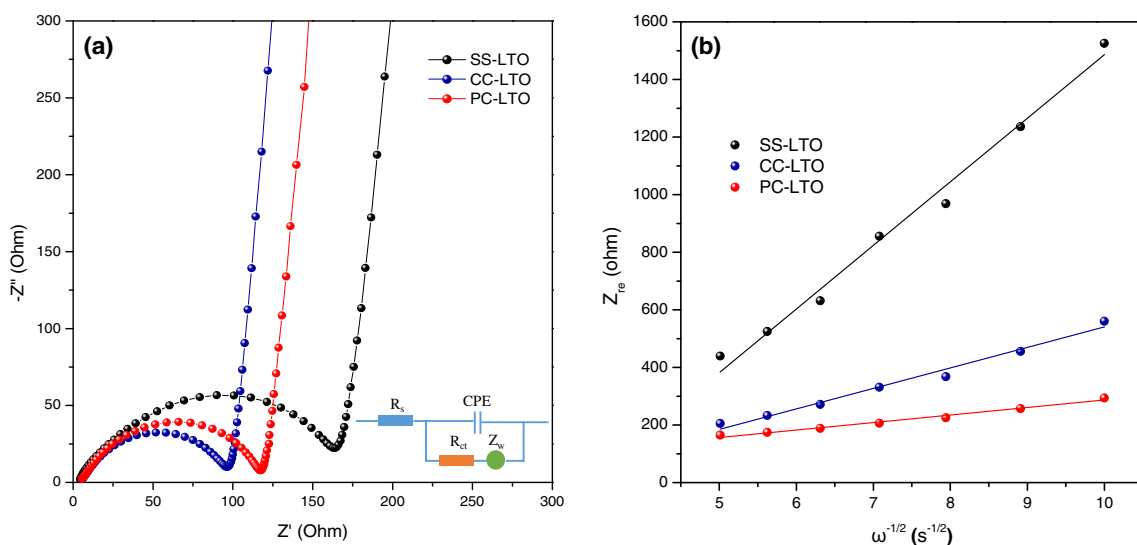

Fig. 10 a Nyquist plots and **b** graph of Z_{re} plotted against $\omega^{-1/2}$ for the SS-LTO, CC-LTO, and PC-LTO anode materials

Table 3 Impedance parameters of the as-prepared SS-LTO, CC-LTO, and PC-LTO samples

Sample	$R_s/(\Omega\ cm^{-2})$	$R_{ct}/(\Omega\ cm^{-2})$	$\sigma/(\Omega\ cm^{-2}\ s^{-1/2})$	$D/(cm^2\ s^{-1})$
SS-LTO	2.637	133.2	220.82	6.18×10^{-14}
CC-LTO	3.944	75.12	71.29	5.93×10^{-13}
PC-LTO	3.885	91.49	26.21	4.39×10^{-12}

treatment. As demonstrated in Table 3, the D value of PC-LTO is 71.04 and 7.40 times larger than that of the SS-LTO and CC-LTO electrodes, respectively. This improved lithium ion diffusion coefficient of PC-LTO should be ascribed to the post-calcination, which gives rise to the reduced particle size and abundant pores, indicating the short distance of electron/lithium ion transportation within the particles and rich transmission paths for facile lithium ion insertion and extraction.

Conclusions

The influence of post-calcination treatment on the spinel LTO anode material has been investigated combining with a ball-milling-assisted rheological phase reaction method. The SEM, particle size, TEM, and nitrogen-adsorption analyses indicate that the post-calcination treatment does not increase the particle size notably but creates many gaps and pores instead, which are beneficial for lithium ion diffusion. Electrochemical results suggest that PC-LTO anode material exhibits the optimal electrochemical properties. A large capacity of 167.9 mAh g^{-1} can be retained after 100 cycles at 1 C rate, with no significant capacity fading. Even at 20 C, the PC-LTO still delivers a high charge specific capacity of 124.5 mAh g^{-1} after 50 cycles, while the corresponding values for CC-LTO and SS-LTO are 112.9 and 43.9 mAh g^{-1}. Moreover, the results of EIS confirm that the PC-LTO anode presents an improved lithium ion diffusion coefficient, showing the obvious advantage for electrode kinetics over CC-LTO and SS-LTO. Thus, the post-calcination treatment is responsible for the improvements of capacity and high-rate capability. All the results indicate that this post-calcination strategy is a promising method to improve the electrochemical properties of LTO and it can be further applied in the large-scale manufacture of LTO and other electrode materials with superior high-power performance.

References

1. Ohzuku T, Ueda A, Yamamoto N (1995) J Electrochem Soc 142:1431
2. Chen ZH, Belharouak I, Sun YK, Amine K (2013) Adv Funct Mater 23:959
3. Chen CH, Vaughey JT, Jansen AN, Dees DW, Kahaian AJ, Goacher T, Thackeray MM (2001) J Electrochem Soc 148:A102
4. Ma J, Wang C, Wroblewski S (2007) J Power Sources 164:849
5. Li X, Qu MZ, Huai YJ, Yu ZL (2010) Electrochim Acta 55:2978
6. Lin C, Fan X, Xin Y, Cheng F, Lai MO, Zhou H, Lu L, Mater J (2014) Chem A 2:9982
7. Kavan L, Prochazka J, Spitler TM, Kalbac M, Zukalova MT, Drezen T, Gratzel M (2003) J Electrochem Soc 150:A1000
8. Ni H, Fan LZ (2012) J Power Sources 214:195
9. Zhang Y, Zhang C, Lin Y, Xiong DB, Wang D, Wu X, He D (2014) J Power Sources 250:50
10. Zhu GN, Liu HJ, Zhuang JH, Wang CX, Wang YG, Xia YY (2011) Energy Environ Sci 4:4016
11. Wang YQ, Guo L, Guo YG, Li H, He XQ, Tsukimoto S, Ikuhara Y, Wan LJ (2012) J Am Chem Soc 134:7874
12. Kubiak P, Garcia A, Womes M, Aldon L, Fourcade JO, Lippens PE, Jumas JC (2003) J Power Sources 119:626
13. Yang G, Su Z, Fang H, Yao Y, Li Y, Yang B, Ma W (2013) Electrochim Acta 93:158
14. Yuan T, Cai R, Shao Z (2011) J Phys Chem C 115:4943
15. Matsui E, Abe Y, Senna M (2008) J Am Ceram Soc 91:1522
16. Lin CY, Duh JG (2011) J Alloys Compd 509:3682
17. Lin JY, Hsu CC, Ho HP, Wu SH (2013) Electrochim Acta 87:126
18. Mosa J, Vélez JF, Lorite I, Arconada N, Aparicio M (2012) J Power Sources 205:491
19. Hao YJ, Lai QY, Liu DQ, Xu ZU, Ji XY (2005) Mater Chem Phys 94:382
20. Prakash AS, Manikandan P, Ramesha K, Sathiya M, Tarascon JM, Shukla AK (2010) Chem Mater 22:2857
21. Yuan T, Wang K, Cai R, Ran R, Shao Z (2009) J Alloys Compd 477:665
22. Marinaro M, Nobili F, Tossici R, Marassi R (2013) Electrochim Acta 89:555
23. Liu J, Li X, Yang J, Geng D, Li Y, Wang D, Li R, Sun X, Cai M, Verbrugge MW (2012) Electrochim Acta 63:100
24. Hsieh CT, Chang BS, Lin JY, Juang RS (2012) J Alloys Compd 513:393
25. Yin SY, Song L, Wang XY, Zhang MF, Zhang KL, Zhang YX (2009) Electrochim Acta 54:5629
26. Cao X, Zhang J (2014) Electrochim Acta 129:305
27. Cao YL, Yu LH, Li T, Ai XP, Yang HX (2007) J Power Sources 172:913
28. Liu DZ, Hayes W, Kurmoo M, Dalton M, Chen C (1994) Physica C 1203:235–240
29. Aldon L, Kubiak P, Womes M, Jumas JC, Olivier-Fourcade J, Tirado JL, Corredor JI, Perez Vicente C (2004) Chem Mater 16:5721
30. Julien CM, Zaghib K (2004) Electrochim Acta 50:411
31. Nakazawa T, Grismanos V, Yamaki D, Katano Y, Aruga T (2003) Nucl Inst Methods Phys Res B 206:166
32. Jović N, Vučinić-Vasić M, Kremenović A, Antić B, Jovalekić Č, Vulić P, Kahlenberg V, Kaindl R (2009) Mater Chem Phys 116:542
33. Inaba M, Yoshida H, Ogumi Z (1996) J Electrochem Soc 143:2572
34. Yuan T, Yu X, Cai R, Zhou Y, Shao Z (2010) J Power Sources 195:4997
35. Bai YJ, Gong C, Lun N, Qi YX, Mater J (2013) Chem A 1:89
36. Tang H, Zhu J, Ma C, Tang Z (2014) Electrochim Acta 144:76
37. Lai C, Dou YY, Li X, Gao XP (2010) J Power Sources 195:3676
38. Li X, Lai C, Xiao CW, Gao XP (2011) Electrochim Acta 56:9152
39. Ding Y, Li GR, Xiao CW, Gao XP (2013) Electrochim Acta 102:282
40. Li JR, Tang ZL, Zhang ZT (2006) Chem Phys Lett 418:506
41. Zhang H, Li GR, An LP, Yan TY, Gao XP, Zhu HY (2007) J Phys Chem C 111:6143
42. Liu GQ, Kuo HT, Liu RS, Shen CH, Shy DS, Xing XK, Chen JM (2010) J Alloys Compd 496:512
43. Chou SL, Wang JZ, Liu HK, Dou SX (2011) J Phys Chem C 115:16220